AMI & KPI programs

| Program ID	TAC	AMI or KPI	Instrument	Interferometry Fraction (%)	PI + co-PI	Allocated Time	Title	Link
1843	GO 1	AMI	NIRISS	100%	Jens Kammerer & Tomas Stolker	2.5	Cloud composition and origin of the reddest known sub-stellar companion HD 206893 B	https://www.stsci.edu/jwst/science-execution/program-information?id=1843
2297	GO 1	AMI	NIRISS	100%	Tomas Stolker	5.1	Unveiling formation signatures in the atmosphere of beta Pictoris c	https://www.stsci.edu/jwst/science-execution/program-information?id=2297
1902	GO Calibration 1	KPI	NIRCam	100%	Kammerer, Pueyo, Sivaramakrishnan	4.3	High Resolution, High Contrast Kernel Phase Imaging with NIRCam	https://www.stsci.edu/jwst/science-execution/program-information?id=1902
2473	GO 1	KPI	NIRCam	100%	Loic Albert & Michael Meyer	38.8	Multiplicity Survey of 20 Y Dwarfs with NIRCam Kernel Phase Interferometry	https://www.stsci.edu/jwst/science-execution/program-information?id=2473
1911	GO 1	KPI	MIRI	50%	Susan Mullaly	24.6	A Search for the Giant Planets that Drive White Dwarf Accretion	https://www.stsci.edu/jwst/science-execution/program-information?id=1911
1189/1230	GTO	KPI	NIRISS	100%	Loic Albert	3.0	Search for a companion around 2 Y dwarfs	https://www.stsci.edu/jwst/science-execution/program-information?id=1189 https://www.stsci.edu/jwst/science-execution/program-information?id=1230
1200	GTO	AMI (+KPI?)	NIRISS	100%	Julien Rameau	8.3	Architecture of Directly-imaged Extrasolar Planetary Systems	https://www.stsci.edu/jwst/science-execution/program-information?id=1200
1242	GTO	AMI	NIRISS	100%	Doug Johnstone	15.8	Planets in Formation and Exozodiacal Disks	https://www.stsci.edu/jwst/science-execution/program-information?id=1242
1260	GTO	AMI	NIRISS	100%	Saavik Ford	4.8	NGC 1068 as Proving Ground for NIRISS AMI	https://www.stsci.edu/jwst/science-execution/program-information?id=1260
1349	ERS	AMI	NIRISS	50%	Ryan Lau	16.9	Establishing Extreme Dynamic Range with JWST: Decoding Smoke Signals in the Glare of a Wolf-Rayet Binar	https://www.stsci.edu/jwst/science-execution/program-information?id=1349
1386	ERS	AMI	NIRISS	10%	Hinkley, Skemer & Biller	54.8	High Contrast Imaging of Exoplanets and Exoplanetary Systems with JWST	https://www.stsci.edu/jwst/science-execution/program-information?id=1386
1373	ERS	AMI	NIRISS	1%	Imke de Pater	40.9	ERS observations of the Jovian System as a demonstration of JWST's capabilities for Solar System science	https://www.stsci.edu/jwst/science-execution/program-information?id=1373
2509	AR 1	KPI	All?	100%	Samuel Factor	0.0	Kernel-Phase Detection Limits for Planet Discovery with JWST	https://www.stsci.edu/jwst/science-execution/program-information?id=2509
1093	Commissioning	AMI & KPI	NIRISS	100%	Anand Sivaramakrishnan	7.5	Commissioning of the AMI mode, including 4 KPI targets	https://www.stsci.edu/cgi-bin/get-proposal-info?id=1093&observatory=JWST
					total (fraction x time)	**116.739**		

Note: This color means parameter is of interest

/Users/albert/Space/udm/articles/KernelPhaseJWSTCycle1/AMI_KPI_programs
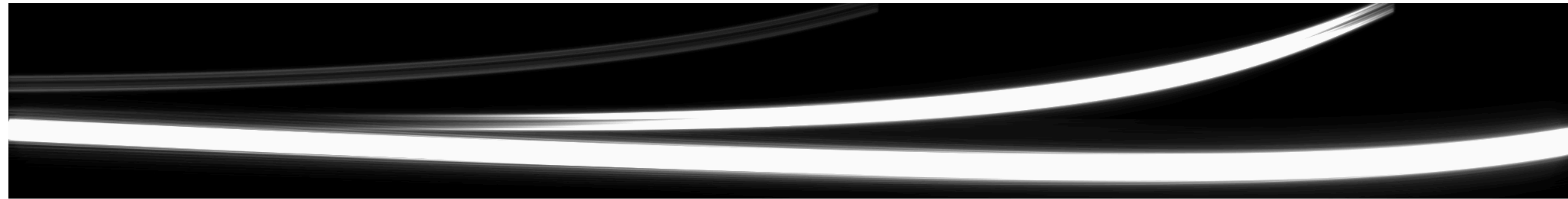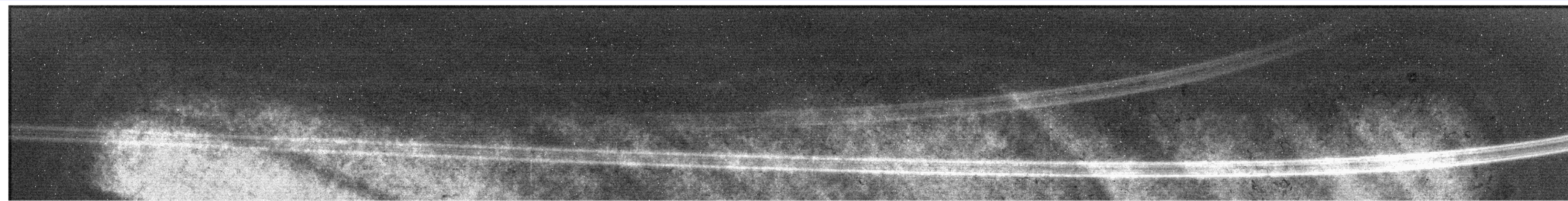
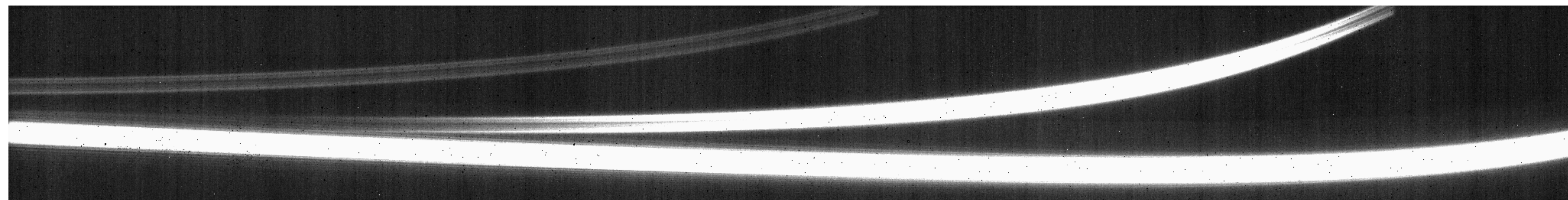# 1/f

Loic Albert

SOSS Simulation Example
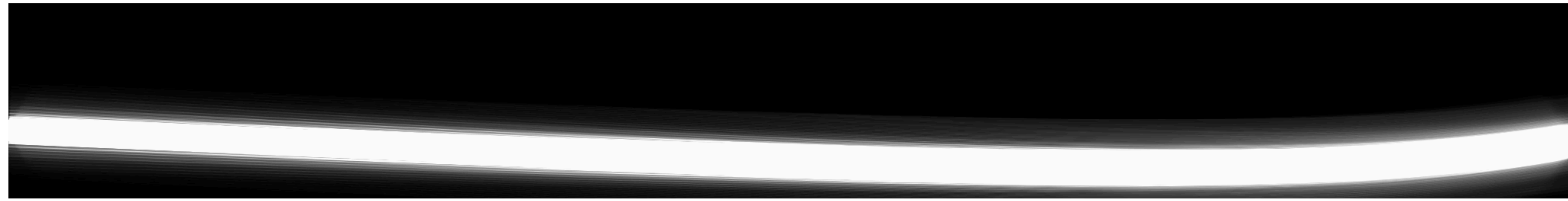
Noiseless
oversampled
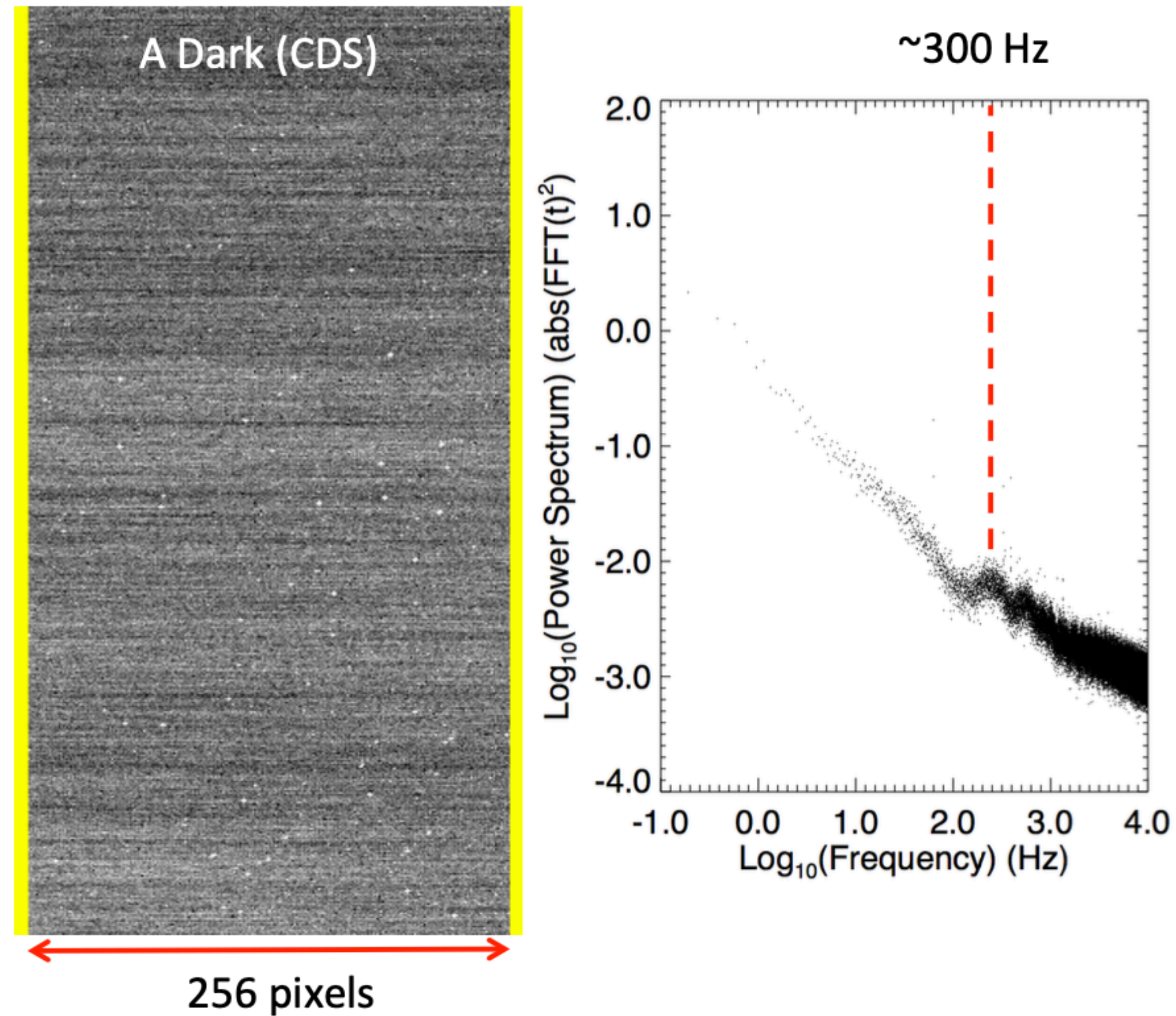order by order

Noiseless
native pixel size
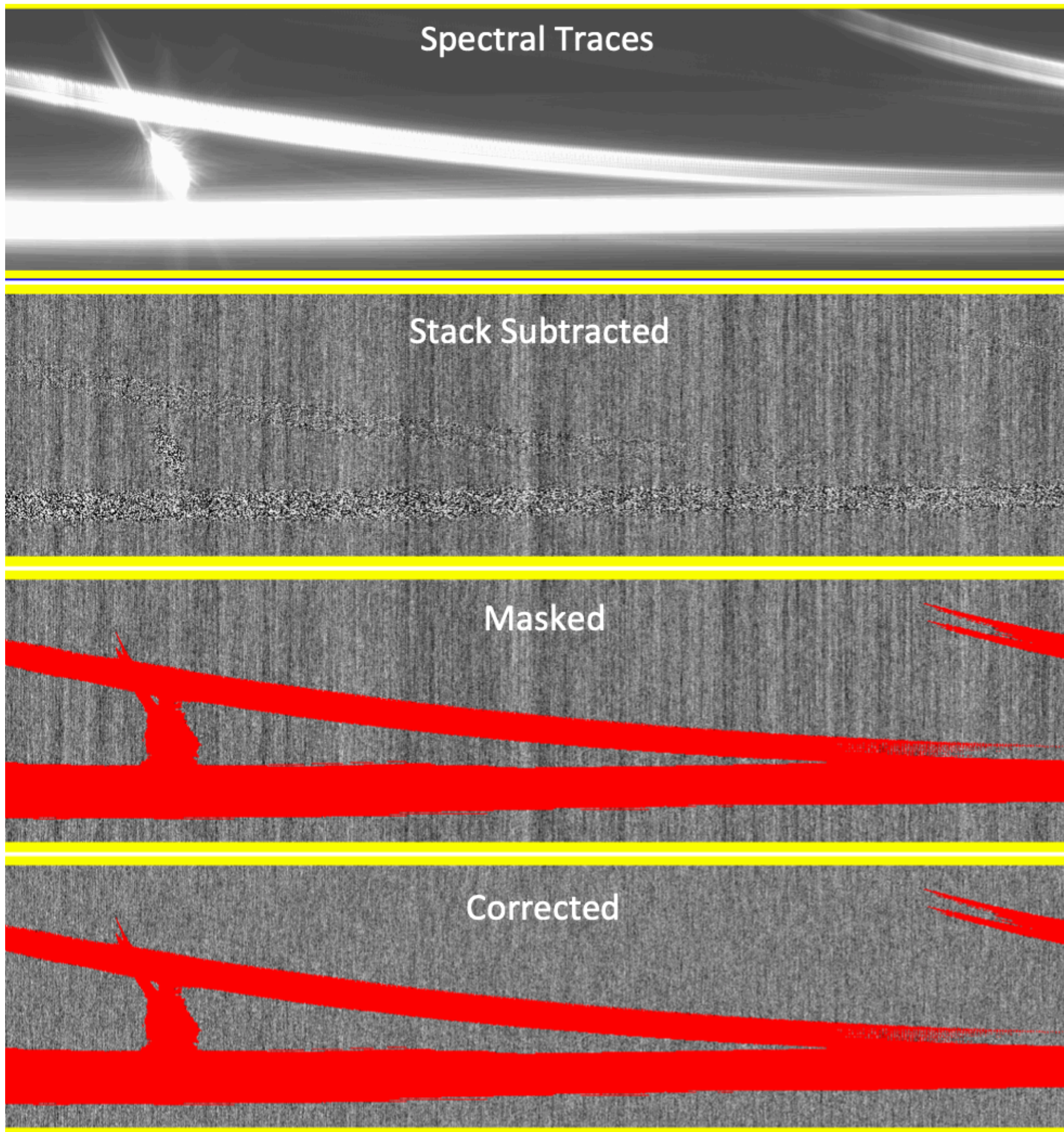DMS format

Noisy
native pixel size
DMS format

**Processed thru
DMS (rateints)**
native pixel size
1 image / integration

1/f noise

1/f Noise

A Dark (CDS)

256 pixels

~300 Hz

In-house (not in DMS) method to correct 1/f

Spectral Traces

Stack Subtracted

Masked

Corrected

Trace Simulation (GJ 1214b)

- Assumes the existence of a deep stack
- Needs a "threshold" parameter to establish pixels to reject from fit (good pixel > threshold)
- Currently use mean of un-masked pixel, column by column. Can think of more fancy fits and quantify them.

Cross-hatching

NIRISS detector

numpy (van der Walt et al. 2011), scipy (Virtanen et al. 2020), pysynphot (Lim et al. 2015), ncdhas, photutils (Bradley et al. 2016), matplotlib (Hunter 2007).

Appendix A
Detailed Characterization of Subpixel Crosshatching

Here, we primarily study the subpixel behavior of the A5 detector because it is used for for the NIRCam grism time-series spectroscopy mode, covering 2.4–5.0 μm with a plate scale of 63 mas px^{-1} (Greene et al. 2017). The flat field of the A5 detector has a pronounced crosshatch pattern, as shown in Figures 1 and 16. The patterns are located at 23°.1, 90°.9, and 158°.6 counterclockwise (CCW) from the $+X$ direction of the detector. The angles between these lines are 67°.8, 67°.7 and 44°.5. These angles and patterns can be analyzed with a 2D power spectrum, as shown in Figure 16.

The angles of the crosshatch patterns are determined by the crystal pattern of HgCdTe. HgCdTe has a zincblende structure with tetrahedral bond angles where each Hg or Cd atom is surrounded by four Te atoms (Gemain et al. 2012). HgCdTe detectors are manufactured using molecular beam epitaxy upon a substrate, a process that can result in topological defects with peak-to-valley amplitudes of 5–20 nm in height variations (Chang et al. 2008).

The surface morphology of the HgCdTe crystal shows that the crosshatch patterns are oriented along the intersection of the (211) growth plane of the crystal and the eight HgCdTe slip planes. The relative angles of the HgCdTe slip planes and (211) growth plane are 44°.42, 67°.79, and 67°.79 (Chang et al. 2008), very close to the observed crosshatch angles. A projection of zincblende structure is shown in Figure 16 at the same orientation of the power spectrum structure. The similarity between the crosshatch patterns in the flat field and the topological variations observed in Chang et al. (2008) leads to the likely conclusion that the surface variations lead to quantum efficiency variations. Thus, the crosshatch pattern is most likely related to the crystal lattice structure of the HgCdTe substrate and not to the pixel circuitry or readout electronics.

The crosshatch structure of the detectors extends down to the subpixel level, so it will not be fully corrected with a flat-field division. This subpixel structure has been imaged with microscopy on a candidate Euclid HgCdTe detector (Shapiro et al. 2018). Atomic force microscopy shows topological features that are approximately 1.2 μm in width (Chang et al. 2008) compared to the 18 μm pixel sizes.
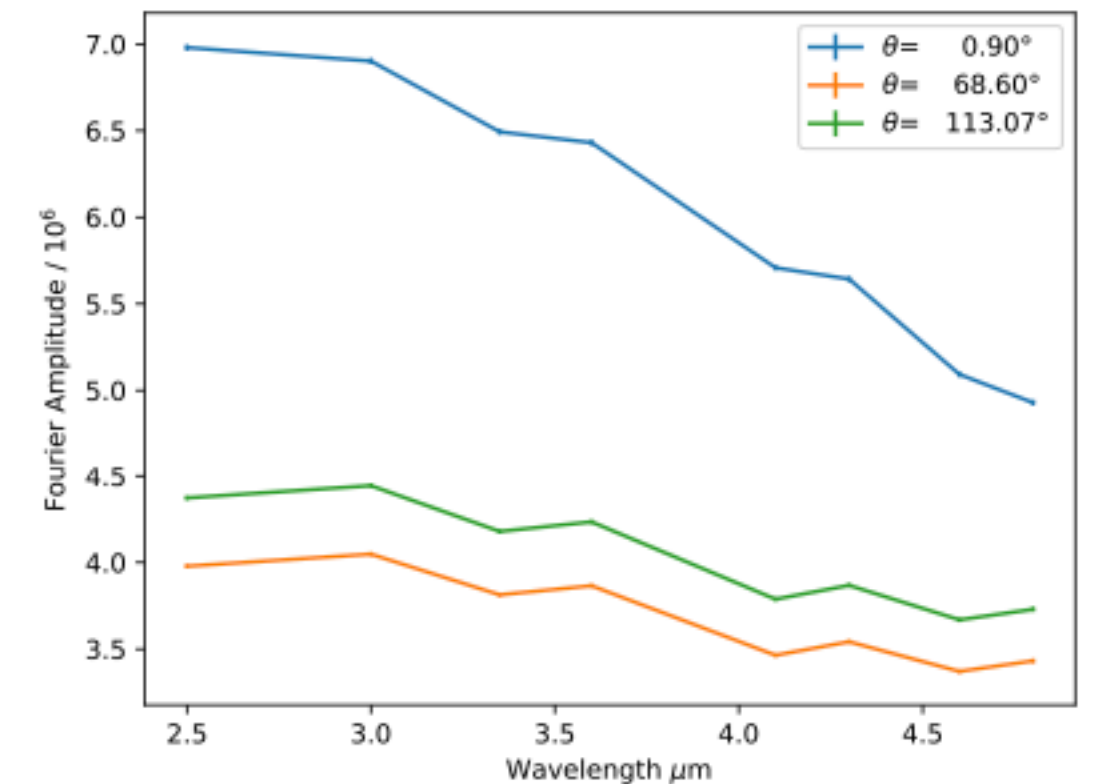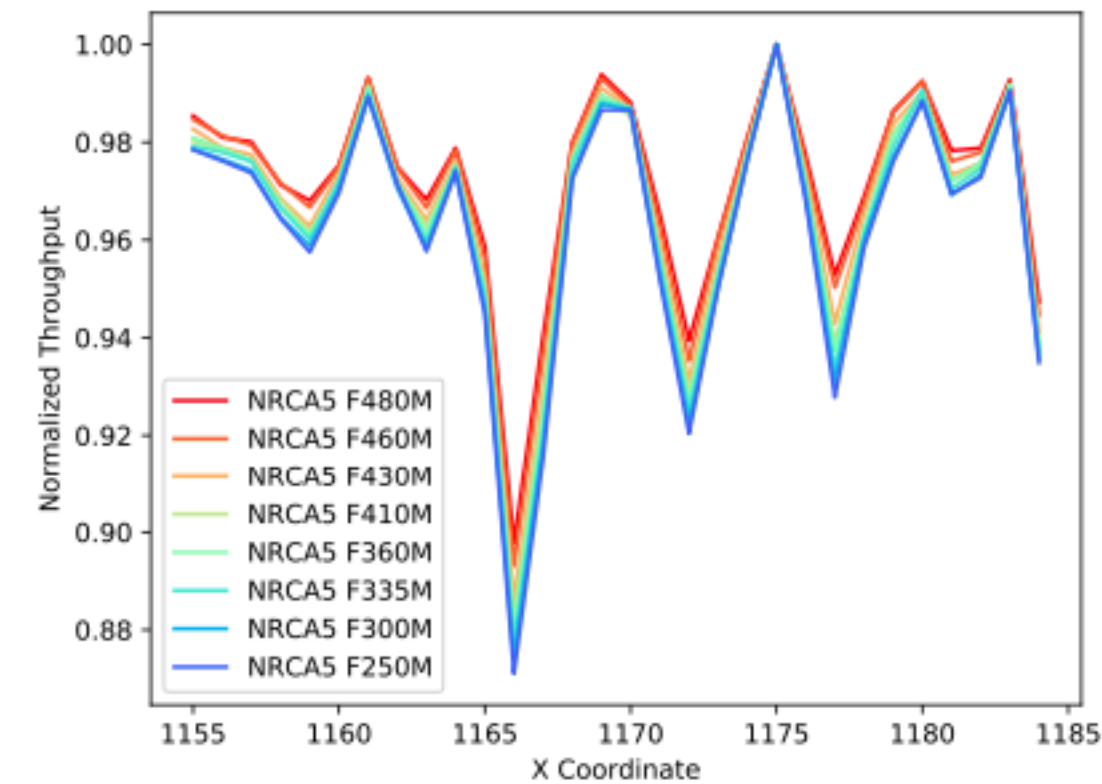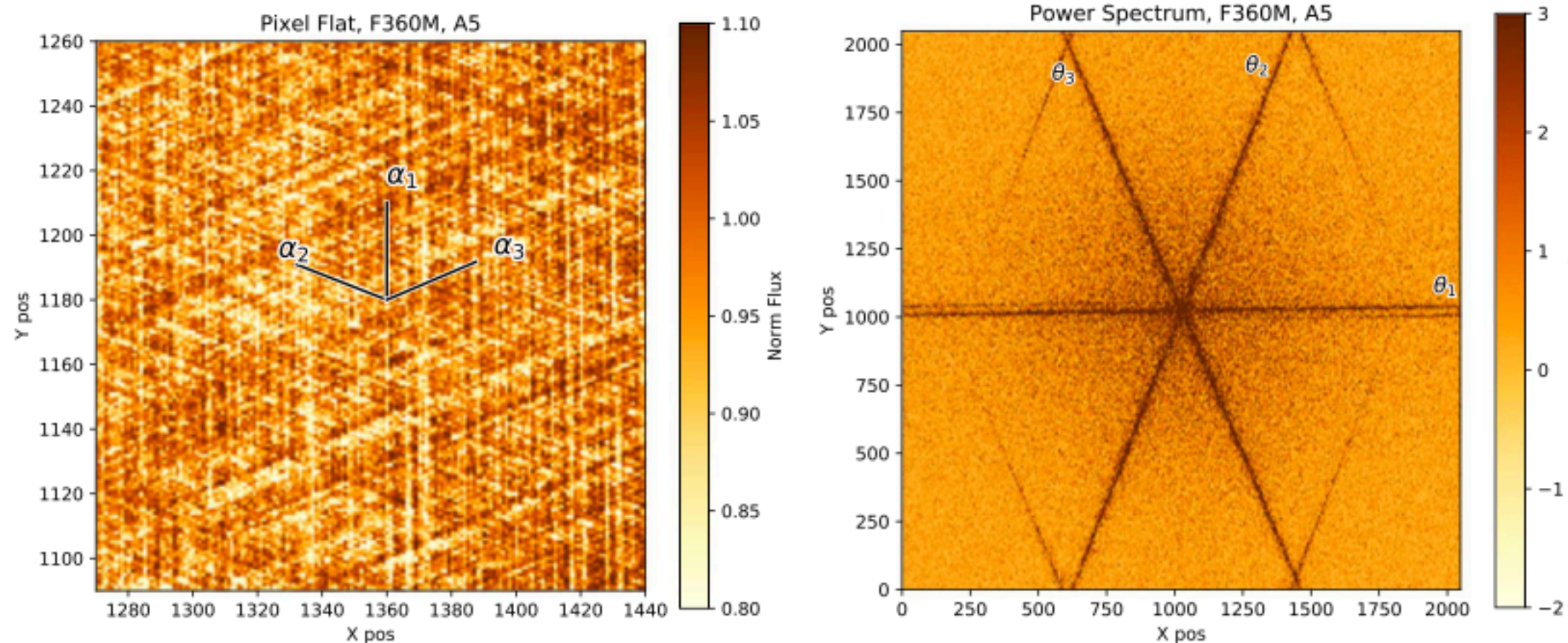

Figure 17. The crosshatch pattern changes as a function of wavelength likely because the shorter wavelengths resolve the structure better. In other words, the crosshatch pattern becomes slightly blurred at longer wavelengths due to diffraction. The shorter wavelengths have deeper crosshatch troughs in a flood-illuminated flat field (left). The flat fields are shown here for the A5 detector, the same as shown in Figure 16. The sharper crosshatch features at shorter wavelengths show up as larger Fourier amplitudes (right).

The width of the structures can also be estimated from the behavior for crosshatch lines as they cross pixel boundaries (Ninan et al. 2019). We estimate that the crosshatch pattern oriented at 90°.9 crosses 1 horizontal pixel for every 64 vertical pixels. While crossing the boundary, there are ≈ 38 rows where a sharp feature in the crosshatch pattern spans 2 pixels instead of 1. The sharp feature is traced by the pixels that drop significantly below the mean flat-field value in a local region. If the sharp feature in the crosshatch pattern has a tophat shape, then these 38 rows where the pattern spans two pixels imply a tophat full width of 0.6 pixels or a physical width of 10.8 μm for an 18 μm pixel pitch. This is more than twice the estimate from Ninan et al. (2019) for an HgCdTe used on the Habitable Zone Planet Finder (HPF) instrument. We expect that the width of the crosshatch pattern varies among detectors or that a tophat function is a poor approximation of the actual subpixel response of this detector. Within NIRCam detectors, there are large variations in the strength and orientation of crosshatch features.

The crosshatch pattern is wavelength dependent, as seen in Figure 17. Here, the flat field for the A5 detector as well as the 2D Fourier amplitude are shown, which area the same data as used in Figure 16. The throughput variations are largest for short wavelengths (better resolving crystal structures) and smallest for the long wavelengths. This is visible both in the throughput cross section of the flood-illuminated flat field and the Fourier amplitude of the crosshatch as a function of wavelength. We find a steeper wavelength dependence for the crosshatch pattern near 0°.9 from horizontal in the frequency domain or 0°.9 from vertical in the length domain.
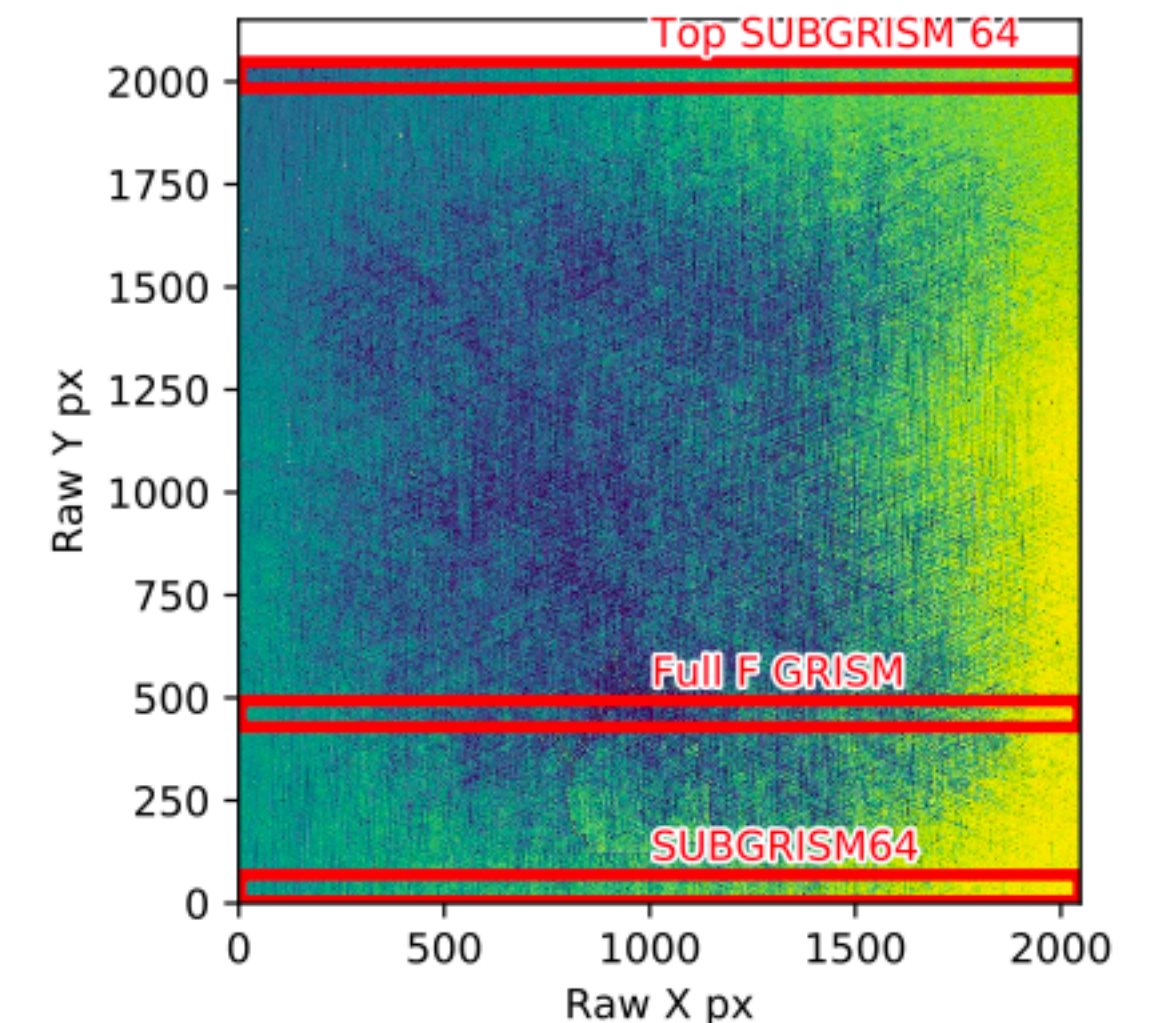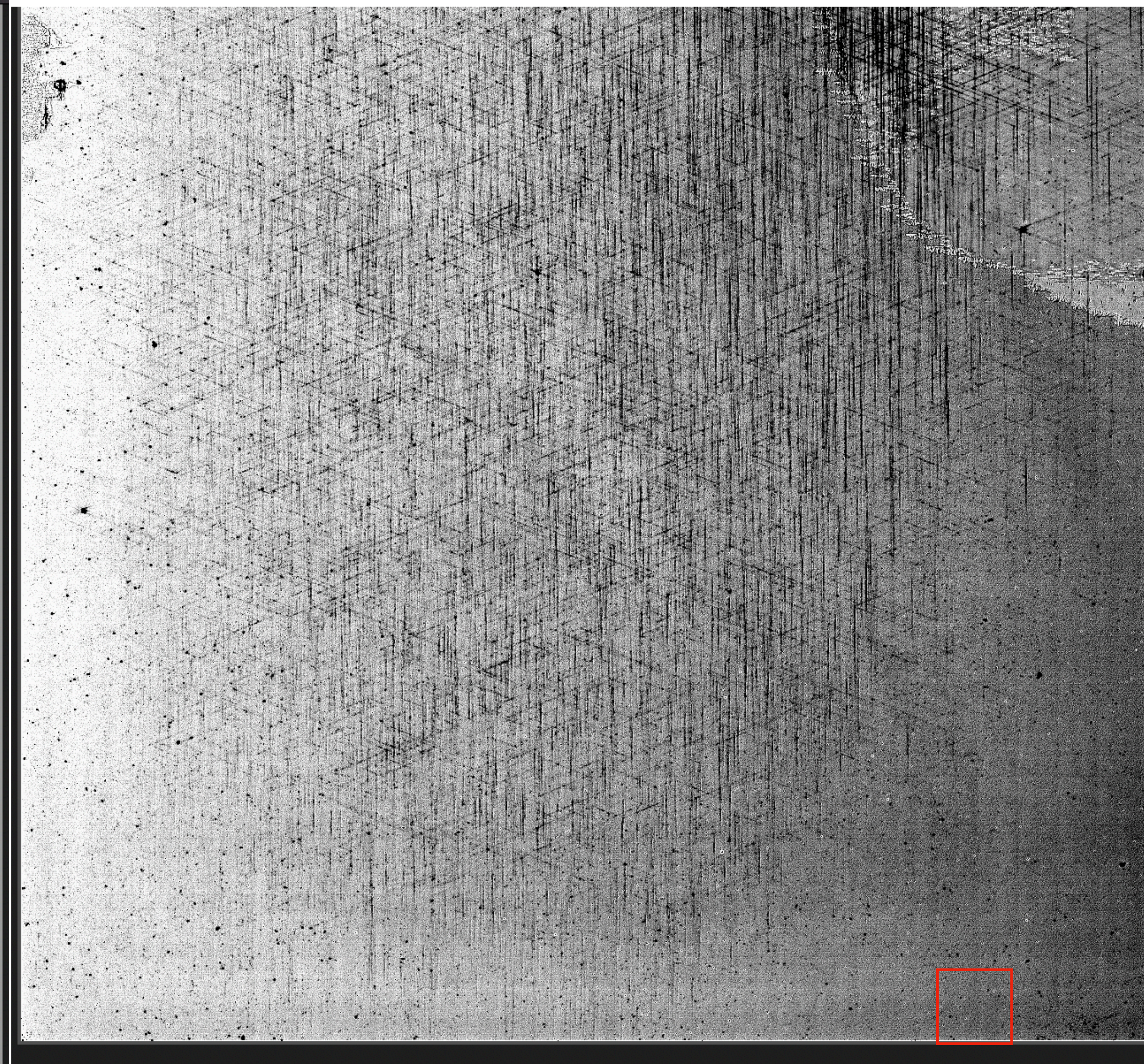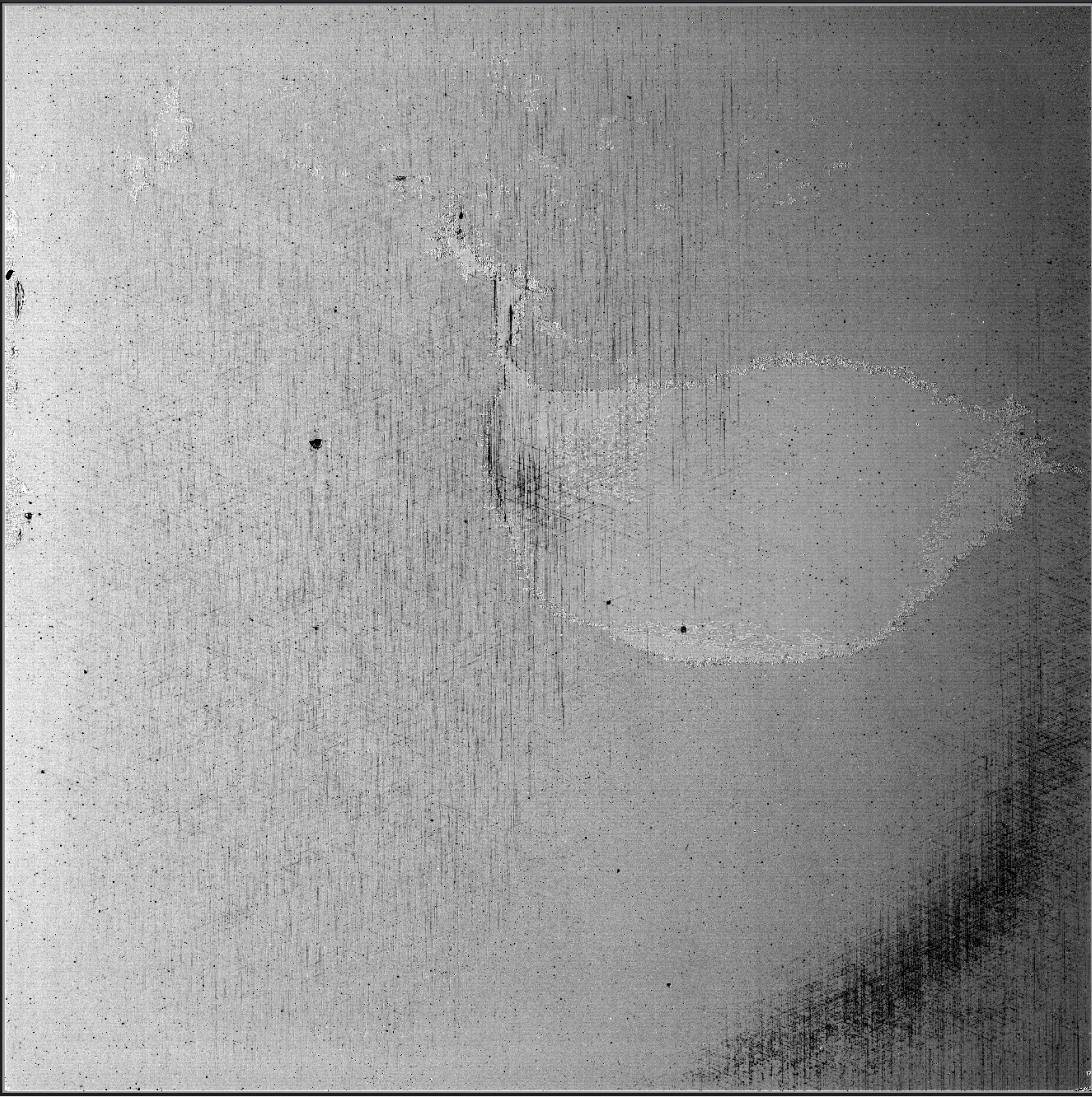

Figure 18. The three regions considered in Section 3.2 are shown in a full-frame flat-field image of the A5 detector.

Appendix C
Charge-trapping Schematic

All HgCdTe detectors show a signal after bright illumination even when the illumination is removed; this is called persistence. The physical mechanism that explains persistence is that charges are trapped in the depletion region after

Figure 16. Pixel Flat, F360M, A5 (left) and Power Spectrum, F360M, A5 (right).

AMI 80x80
(1045,1)

Target Acquisition
AMI & SOSS

https://jwst-docs.stsci.edu/jwst-near-infrared-imager-and-slitless-spectrograph/niriss-operations/niriss-target-acquisition

Pipeline steps

DMS Stage 1 steps

```
These are the default DMS steps for stage 1.
Default pipeline.calwebb_detector1 steps

        input = self.group_scale(input)
        input = self.dq_init(input)
        input = self.saturation(input)
        input = self.ipc(input)
        input = self.superbias(input)
        input = self.refpix(input)
        input = self.linearity(input)
        input = self.dark_current(input)
        input = self.jump(input)
        input = self.ramp_fit(input)
        input = self.gain_scale(input)
```